Structure and primase-mediated activation of a bacterial dodecameric replicative helicase

Alexandre Bazin, Mickael V Cherrier, Irina Gutsche, Joanna Timmins, Laurent Terradot

Nucleic Acids Research Advance Access published August 11, 2015

Nucleic Acids Research, 2015 **1**
doi: 10.1093/nar/gkv792

Structure and primase-mediated activation of a bacterial dodecameric replicative helicase

Alexandre Bazin[1], Mickaël V. Cherrier[1], Irina Gutsche[2], Joanna Timmins[3,4,5] and Laurent Terradot[1,*]

[1]CNRS, UMR 5086 Bases Moléculaires et Structurales de Systèmes Infectieux, Institut de Biologie et Chimie des Protéines, 7 Passage du Vercors, F-69367, Lyon, France. Université de Lyon, F-69622, Lyon, France; Université Claude Bernard Lyon 1, F-69622, Villeurbanne, France, [2]Unit of Virus Host-Cell Interactions, UJF-EMBL-CNRS, UMI3265, F-38044 Grenoble Cedex 9, France, [3]Univ. Grenoble Alpes, Institut de Biologie Structurale, F-38044 Grenoble, France, [4]CNRS, Institut de Biologie Structurale, F-38044 Grenoble, France and [5]CEA, Institut de Biologie Structurale, F-38044 Grenoble, France

Received May 18, 2015; Revised July 20, 2015; Accepted July 22, 2015

ABSTRACT

Replicative helicases are essential ATPases that unwind DNA to initiate chromosomal replication. While bacterial replicative DnaB helicases are hexameric, *Helicobacter pylori* DnaB (*Hp*DnaB) was found to form double hexamers, similar to some archaeal and eukaryotic replicative helicases. Here we present a structural and functional analysis of *Hp*DnaB protein during primosome formation. The crystal structure of the *Hp*DnaB at 6.7 Å resolution reveals a dodecameric organization consisting of two hexamers assembled via their N-terminal rings in a stack-twisted mode. Using fluorescence anisotropy we show that *Hp*DnaB dodecamer interacts with single-stranded DNA in the presence of ATP but has a low DNA unwinding activity. Multi-angle light scattering and small angle X-ray scattering demonstrate that interaction with the DnaG primase helicase-binding domain dissociates the helicase dodecamer into single ringed primosomes. Functional assays on the proteins and associated complexes indicate that these single ringed primosomes are the most active form of the helicase for ATP hydrolysis, DNA binding and unwinding. These findings shed light onto an activation mechanism of *Hp*DnaB by the primase that might be relevant in other bacteria and possibly other organisms exploiting dodecameric helicases for DNA replication.

INTRODUCTION

DNA replication is an essential process in all organisms and consists of the faithful duplication of the genetic material to be transmitted to daughter cells. Initiation of DNA replication relies on helicases, key motor proteins that unwind DNA so that it can be used as a template for DNA polymerases (1). Replicative helicases are hexameric ring-shaped proteins that hydrolyse ATP and unwind double-stranded DNA (dsDNA), with one strand running through the central cavity of the hexamer and the other being excluded from the ring. In bacteria, the replicative helicase DnaB functions as a hexamer to unwind dsDNA in the 5′ to 3′ direction (1).

The DnaB monomer consists of an N-terminal domain (NTD, comprising a head and a helical hairpin) and a C-terminal RecA type ATPase domain (CTD) associated through a linker (Figure 1A) (2). The NTDs and CTDs assemble into separate rings (namely NTD- and CTD-rings) that have different symmetries and form a two-tiered hexamer (3,4). In the absence of a ligand, the NTD-ring adopts a trimer of dimers organization (4) (described as 'dilated' (5)), which opens a large central channel in the helicase. In the presence of nucleotides, the NTD can also adopt a triskel like structure (described as 'constricted'), a conformation compatible with interaction with the τ subunit of the polymerase (5).

Because DnaB forms closed rings, threading of single-stranded DNA (ssDNA) through the central channel of DnaB requires ring-breaking or ring-making mechanisms during initiation of replication (6). In addition, because of their polarity, two hexamers of DnaB must be positioned in opposite directions at the origin on each of the DNA forks for replication to proceed bi-directionally (7). In some bacteria, loading of the helicase is assisted by AAA+ helicase loaders such as DnaC in *Escherichia coli* or DnaI in *Bacillus subtilis* (*Bsu*DnaI) (7). *E. coli* DnaC forms a 6:6 complex with *Ec*DnaB (8,9). The interaction with the loader opens the *Ec*DnaB rings into a lock-washer conformation and triggers a helical conformation of the overall complex, thereby providing an entry point for ss-

*To whom correspondence should be addressed. Tel: +33 472722652; Fax: +33 472722604; Email: laurent.terradot@ibcp.fr

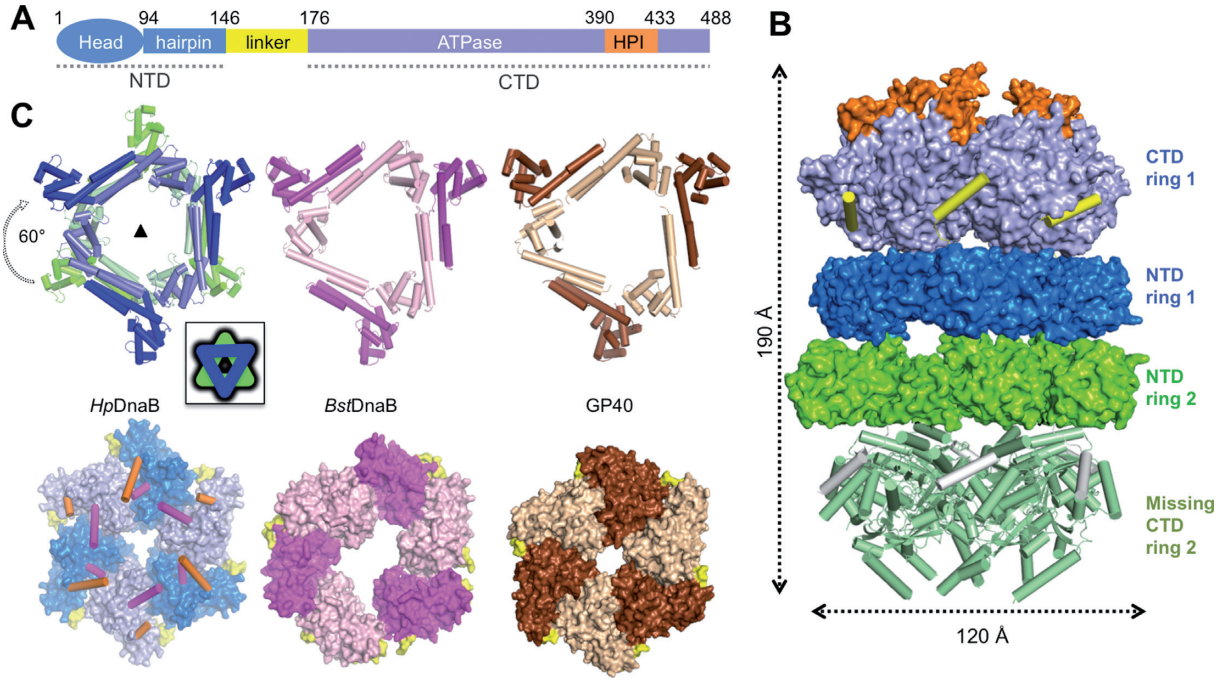

Figure 1. Crystal structure of *Hp*DnaB dodecamer. (**A**) Schematic representation of *Hp*DnaB domain organization. (**B**) Surface representation of His-*Hp*DnaB crystal structure with one hexamer colored according to the domain organization described in A) and the second one in green. The second CTD-ring, absent in the crystal structure has been modeled and is shown as a cartoon. (**C**) Top panels, structures of NTD-rings of His-*Hp*DnaB, apo *Bst*DnaB and GP40. The inset depicts a schematic representation of the apparent six-fold symmetry of His-*Hp*DnaB NTD-rings. Bottom panels, surface representation of *Hp*DnaB, apo *Bst*DnaB and GP40 CTD-ring structures. Subunits are colored in alternating shades for clarity, linker helices are colored in yellow, HPI helices α15 (orange) and α16 (magenta) are shown as cylinders.

DNA (10). A non-planar architecture has also been observed in the pre-priming complex composed of *Bsu*DnaI and *Bacillus stearothermophilus* helicase (*Bst*DnaB), as well as the helicase-binding domain (HBD) of the primase (*Bst*DnaG^{HBD}) (11), suggesting that helicase loading might depend on a transition of the helicase from planar to non-planar conformation induced or stabilized by the AAA+ helicase loader (10,11).

During replication, the active form of DnaB is a complex of the helicase with up to three DnaG primases, named the primosome. Transition from a loaded helicase•helicase-loaders•primase complex to an active unwinding primosome requires additional conformational changes of the helicase. Closing of the helicase rings is likely facilitated by nucleotide and ssDNA binding since the translocation conformation of DnaB on ssDNA is also spiral (12). *Bst*DnaG^{HBD} interaction with the pre-primed *Bst*DnaB•*Bsu*DnaI complex resulted in a ternary complex that might be loaded onto the replication fork (11). In *E. coli*, primer synthesis by DnaG in complex with DnaB releases DnaC (13) and stimulates DnaB helicase and ATPase activities (14). Therefore, bacteria appear to have developed different strategies for the formation of primosomes. Moreover, AAA+ loader-dependent primosomes are unlikely to represent a universal strategy since loader homologues have been identified in only a subset of bacterial species (∼20%) (15). Concomitantly, the human pathogen *Helicobacter pylori* does not encode for a DnaC/I homologue. Moreover, *H. pylori* DnaB (*Hp*DnaB) could complement two temperature-sensitive mutants of *E. coli dnaBts* and *dnaCts,* suggesting that *Hp*DnaB was able to bypass DnaC in these cells (16). *Hp*DnaB formed a double hexamer (17) with an architecture remarkably similar to head-to-head double hexamers of some replicative helicases of archaea, yeast and some viruses (7,17). However, the absence of higher resolution structures of dodecameric helicases and the limited resolution of our *Hp*DnaB reconstruction (23 Å) prevented insightful structural comparison. It was also unclear whether such a double hexameric assembly could bind and unwind DNA and what its fate was during primosome formation.

Here, we have solved the crystal structure of the *Hp*DnaB dodecamer at a resolution of 6.7 Å, which reveals that the helicase can assemble as a planar, stack-twisted double hexamer. Using a complementary set of methods, we found that *Hp*DnaB interacts preferentially with ssDNA as a dodecamer in the presence of ATP but is poorly active for DNA unwinding. Interaction with *Hp*DnaG^{HBD} dissociates the helicase dodecamer into single-ringed primosomes that represent a more active form of the helicase for DNA unwinding. We propose that in the absence of a control mechanism by AAA+ loaders, dissociation of the double hexamer of the helicase by the primase represents a key switch to launch DNA replication in *H. pylori* and possibly other replication systems utilizing double hexamer replicative helicases.

MATERIALS AND METHODS

Gene cloning, protein expression and purification

His-*Hp*DnaB was purified as previously described (17) with an N-terminal histidine-tag consisting of 28

amino-acids (MHHHHHHGKPIPNPLLGLDSTENLYFQG). Selenomethionine-substituted His-*Hp*DnaB (His-*Hp*DnaB^{Se}) was produced using the protocol described in (18) and purified as His-*Hp*DnaB (17). For wild-type *Hp*DnaB expression, the DNA sequence of *hpdnab* gene was amplified by polymerase chain reaction (PCR) using the forward primer 5′-agtcatatggatcatttaaagcatttgcag-3′ containing a *Nde*I restriction site (underlined) and reverse primer 5′-atactcgagttcaagttgtaactatatcataatcc-3′ containing a *Xho*I site (underlined). The fragment was inserted into the pACYCDuet-1 vector to produce the pACYC*hpdnab* expression vector. Single point mutations were introduced into pACYC*hpdnab* using the Quick change site directed mutagenesis kit (Stratagene) using manufacturer's protocol. An N-terminal deletion mutant starting at residue 10 (*Hp*DnaB$^{\Delta 9}$) was generated by PCR (forward primer 5′-caccatgttgcaaaacattgaaaggatcgtgc-3′ and same reverse primer than for wild-type) and inserted into pET101/D-TOPO vector (Invitrogen). The sequence encoding for the helicase binding domain of *Hp*DnaG (*Hp*DnaG^{HBD}, residues 415–559) was amplified from *H. pylori* genomic DNA (strain 26695) using the forward 5′-caccgtctcttttcagccttttttaccc-3′ and reverse 5′-tcatatggcgactaattctccttg-3′ primers and inserted into pET151/D-TOPO (Invitrogen) to generate the plasmid pET*hpdnag*^{HBD}.

*Hp*DnaB and mutants were expressed in *E. coli* BL21 Star (DE3) cells (Invitrogen) grown in LB medium with chloramphenicol at 50 μg.l^{-1} (or ampiciline at 100 μg.l^{-1} for *Hp*DnaB$^{\Delta 9}$) at 37°C until OD_{600} = 0.6. Protein expression was induced with 1mM isopropyl β-D-thiogalactopyranoside (IPTG) during 16 h at 20°C. Harvested cells were resuspended in lysis buffer (10 mM phosphate pH 7.5, 200 mM NaCl) with protease inhibitor tablet (complete EDTA-free, Roche), lysozyme (Roche) and DNase I (Sigma-Aldrich). The cells were lysed by sonication and centrifuged at 16 000 g for 20 min. The soluble fraction was diluted four-fold with buffer A and applied onto a HiTrapTM Heparin 5 ml column equilibrated with buffer A (10 mM phosphate pH 7.5, 2 mM βME). The protein was eluted using a 0–100% gradient of buffer B (10 mM phosphate pH 7.5, 1 M NaCl, 2 mM βME). Fractions containing the protein were pooled and applied on a HiTrap Q HP (GE Healthcare) column as a second purification step using the same elution protocol. The protein was concentrated and loaded onto a Superdex 200 10/300 GL gel filtration column (GE Healthcare) equilibrated in 10 mM phosphate pH 7.5, 200 mM NaCl, 2 mM βME.

For *Hp*DnaG^{HBD} expression, *E. coli* BL21 Star (DE3) cells (Invitrogen) carrying the pET*hpdnag*^{HBD} plasmid were grown in LB medium with ampicillin (100 μg.l^{-1}) at 37°C until an OD_{600} of 0.6 and protein expression was induced by adding 1mM IPTG at 20°C overnight. The cells were harvested and resuspended in lysis buffer (50 mM Tris pH 8.0, 200 mM NaCl) with protease inhibitor (Roche), lysozyme (Roche) and DNase I (Sigma). The cells were sonicated and centrifuged at 16 000 g for 20 min at 4°C. The supernatant was applied on a HisTrapTM HP 5 ml (GE Healthcare) pre-equilibrated with buffer C (50 mM Tris pH 8.0, 200 mM NaCl, 1 mM DTT and 5% (v/v) glycerol). The protein was eluted by applying a linear gradient (10–100%) of buffer D (buffer C with 500mM imidazole). Fractions containing *Hp*DnaG^{HBD} were pooled and incubated with TEV protease with 1 mM DTT and 0.5 mM EDTA, and dialyzed overnight against buffer D at 4°C. After TEV cleavage the protein fraction was loaded on the HisTrapTM column and *Hp*DnaG^{HBD} eluted with 10% of buffer B. The protein was injected on a Superdex 200 10/300 GL (GE Healthcare) gel filtration column and eluted with buffer C.

Crystallization, X-ray diffraction data collection and structure determination

Crystals of His-*Hp*DnaB and His-*Hp*DnaB^{Se} were grown at 292 K in polyethylene glycol 3350 26%, 100 mM Tris pH 8.6 and 200 mM lithium sulphate with protein incubated with 1 mM ADP and 1 mM $MgCl_2$. Drops were set-up by mixing 1.5 μl of protein solution (10 mg.ml^{-1}) with 1.5 μl of reservoir solution. Hexagonal crystal forms were obtained after one to two months. Tantalum Bromide derivative crystals were obtained by incubating the crystals for 2 h in the presence of 0.01 mg of $Ta_6Br_{12}^{2+}$ powder (Jena Biosciences Gmbh). Single crystals were harvested and flash frozen in liquid nitrogen (100 K) using the mother liquor supplemented with 10% sucrose for cryoprotection. Two single-wavelength X-ray diffraction data sets (Tant 1 and Tant 2) were collected from a single Tantalum Bromide crystal on beamline Proxima 2a at the synchrotron SOLEIL. His-*Hp*DnaB^{Se} X-ray data were collected on the beamline ID14EH4 at the European Synchrotron Radiation Facility. The diffraction data were indexed and integrated using XDS (19) and scaled with SCALA from the CCP4 program suite (20). To verify that the crystals contained the full-length protein *Hp*DnaB, crystals were dissolved and analyzed on SDS-PAGE.

Structure determination, model building and refinement

The structure of *Hp*DnaB was solved by the single anomalous dispersion method with Tant 1 data collected at the inflection wavelength from a single crystal. The positions of three Tantalum clusters were found using HYSS (21) and were then submitted to Phaser (22), which is integrated in Autosol in PHENIX (23). The experimental map at 7.5 Å resolution was of excellent quality and revealed that the asymmetric unit contained four molecules of *Hp*DnaB. Four molecules of the NTD high-resolution (2.2 Å) crystal structure (residues 1 to 120, (24)) of *Hp*DnaB (*Hp*DnaB^{NTD}) were placed into the electron density map and the second helices of the four NTD α-hairpins were built using COOT (25). These domains were used for NCS averaging using PARROT (26) which improved the electron density map. Two high-resolution (2.5 Å) crystal structures of the CTD (residues 176 to 473 (17)) of *Hp*DnaB could then be placed and fitted into this averaged map. Placing these domains resulted in R_{factor}/R_{free} of 0.30/0.32, respectively, after a first round of refinement with BUSTER TNT (27). The linker helices were placed and the *Helicobacter pylori* insertion (HPI) helices (Figure 1A) were adjusted by rigid body modeling. Density was observed for two helices of the second CTD-ring but the two subunits could not be placed reliably. Soaking the crystals in a solution containing

ssDNA or co-crystallization experiments in various conditions (ssDNA lengths, nucleotides and concentration) did not improve either the resolution or the electron density map corresponding to this region. No ADP molecule could be placed in the nucleotide binding site since no density was observed in the Fo-Fc map with or without NCS averaging. The resulting model was subsequently refined against Tant 2 data set to extend the resolution to 6.7 Å using BUSTER TNT (27) and PHENIX (23). In the final rounds of refinement, a cluster of $Ta_6Br_{12}^{2+}$ could be placed in the density. During refinement, tight geometry constraints were maintained, group B-factors and NCS restraints were used. The final His-*Hp*DnaB model was refined to a resolution of 6.7 Å with R_{factor}/R_{free} of 0.25/0.29 and very good geometry. Data collection, phasing and refinement statistics are shown in Table 1. The model coordinates were deposited in the protein data bank (pdb code 4ZC0).

Size exclusion chromatography (SEC)-Multi-angle light scattering (MALS)

Size exclusion chromatography (SEC) combined with multi-angle light scattering (MALS) and refractometry (RI) experiments were performed with a Shodex KW405–4F size exclusion column equilibrated with 50 mM Tris pH 8.0, 200 mM NaCl, 1 mM DTT and 5% (v/v) glycerol. 12.5 µl of protein samples of *Hp*DnaB or mutants (15 mg.ml^{-1}) and *Hp*DnaG^{HBD} (20 mg.ml^{-1}) were injected onto the column. For samples containing nucleotides the proteins were first incubated with 5 mM ATP or AMPPNP and 5 mM $MgCl_2$ and the buffer was supplemented with 0.5 mM of the corresponding nucleotides and 5 mM $MgCl_2$. For samples of the *Hp*DnaB•*Hp*DnaG^{HBD} complex, the separated proteins were incubated at equal molar amounts at a final concentration of 15 mg.ml^{-1}. For ssDNA complex measurements the protein or complexes were first mixed with a 20mer polydT oligonucleotide at either 45 µM or 75 µM (final concentration). On-line MALS detection was performed with a miniDAWN-TREOS detector (Wyatt Technology Corp., Santa Barbara, CA) using a laser emitting at 690 nm and refractive index measurements were performed using an Optilab T-rex system (Wyatt Technology Corp., Santa Barbara, CA). Weight averaged molar masses were calculated using the ASTRA software (Wyatt Technology Corp., Santa Barbara, CA).

Negative staining electron microscopy and image analysis

*Hp*DnaB sample from SEC-MALS (0.1 mg.ml^{-1}) was applied to the clear side of carbon on a carbon-mica interface and stained with 2% (w/v) uranyl acetate. Images were recorded with a JEOL 1200 EX II microscope at 100 kV and at a nominal 40 000x magnification. Negatives were digitized on a Zeiss scanner (Photoscan TD) to a pixel size of 3.5 Å at the specimen level. 9135 individual particles of *Hp*DnaB were semi-automatically selected with the EMAN boxer routine (28), CTF-corrected with CTFFIND3 (29) and bsoft (30), and low-path-filtered at 15 Å with Spider (31). This data set was subjected to multivariate statistical analysis and classification with Imagic-5 (32).

Small-angle X-ray scattering experiments

SAXS data were recorded on beamline Swing at SOLEIL Synchrotron (Gif sur Yvette, France) at a wavelength of 1.003 Å on a 17 cm × 17 cm low-noise Aviex charge-coupled device detector positioned at a distance of 1800 mm from the sample, with the direct beam off-centered. The useful Q-range was 0.004–0.61 Å^{-1}, where $Q = 4\pi\sin\theta/\lambda$ is the scattering vector, and 2θ is the scattering angle. 50 µl of sample in buffer S (50 mM Tris pH 8.0, 200 mM NaCl, 5% (v/v) glycerol, 1 mM DTT) were injected into a size-exclusion column (Shodex KW405–4F) using an Agilent© HPLC system cooled at 288 K and eluted directly into the SAXS flow through capillary cell at a flow rate of 200 µl.min^{-1}, as previously described (33). Protein and buffer samples were prepared exactly as described for the MALS experiments, i.e. for samples containing nucleotides, the proteins were first incubated with 5 mM ATP or AMPPNP and 5 mM $MgCl_2$ and the buffer was supplemented with 0.5 mM of the corresponding nucleotides and 5 mM $MgCl_2$ to minimize the effects due to ATP hydrolysis. SAXS data were collected online throughout the whole elution time, with a frame duration of 2 s and a dead time between frames of 1 s. A first data set of 90 frames, collected before the void volume, was averaged to account for buffer scattering. A second data set was collected for the sample, from which the 10 frames corresponding to the top of the elution peak were averaged and used for data processing after baseline subtraction (Supplementary Figure S1). Data were processed using the local application FOXTROT (http://www.synchrotron-soleil.fr/Recherche/LignesLumiere/SWING) and analyzed using PRIMUS (34). After processing, Kratky plots were generated to verify if proteins were correctly folded and P(r) functions were calculated (Supplementary Figure S2). Theoretical curves from the models were generated by FoXS (35). Minimal Ensemble Search was performed using MES program (36).

Chemical cross-linking

Cross-linking of *Hp*DnaB and mutants L4A, Q8A, E80A and Δ9 was performed in 20 mM HEPES pH 7.6, 150 mM NaCl, 0.5 mM βME and 5% (v/v) glycerol. For *Hp*DnaB with AMPPNP and ssDNA, the protein was incubated 5 min with AMPPNP (5 mM), $MgCl_2$ (5 mM) and a 20mer polydT ssDNA oligonucleotide (75 µM final concentration) at room temperature before cross-linking. Crosslinking agent ethylene glycol bis(succinimidyl succinate) (EGS) (5 mM final concentration) was added to 20 µg of protein in 20 µl final volume. The mixture was then incubated at room temperature during 10 min and the reaction was quenched with 2 µl of 1M Tris pH 7.5. The samples were run on gradient SDS-PAGE (4–12%) and stained with Coomassie blue for analysis.

ATPase activity

The rate of ATP hydrolysis by *Hp*DnaB (500 nM of monomer) in reaction buffer 20 mM Tris pH 8.0, 100 mM KCl, and 5 mM $MgCl_2$ was measured at a concentration of 5 mM ATP and in the presence and absence of 500 nM single stranded 20mer polydT DNA and/or 500 nM

Table 1. Data collection, phasing and refinement statistics

	Tant 1 ($Ta_6Br_{12}^{2+}$) SOLEIL-Proxima2	Tant 2 ($Ta_6Br_{12}^{2+}$) SOLEIL-Proxima2	SeMet ID14EH4-ESRF
Wavelength (Å)	1.2546	1.2546	0.97239
Space group	$I2_13$	$I2_13$	$I2_13$
Unit-cell parameters (Å)	a = b = c = 284.03 β = 90	a = b = c = 283.47 β = 90	a = b = c = 283.11 β = 90
Resolution limits (Å)	48.8–7.5 (7.91–7.50)	47.2–6.7 (6.93–6.70)	48.6–8.0 (8.43–8.0)
No. of observations	171283 (25533)	308609 (45815)	29801 (4471)
No. of unique observations	5016 (725)	6954 (1005)	4111 (602)
Completeness (%)	99.6 (100)	99.7 (100)	99.5 (100)
Anomalous completeness (%)	99.7(100)	99.8 (100)	99.7(100)
Multiplicity	34.1 (35.2)	44.3 (45.6)	7.2 (7.4)
Anomalous multiplicity	18.1 (18.2)	23.3 (23.6)	3.8 (3.8)
Rmeas	0.13 (> 1)	0.18 (> 1)	0.10 (0.64)
Rpim	0.03 (0.27)	0.03 (0.99)	0.05 (0.23)
Rmerge	0.11 (> 1)	0.17 (> 1)	0.09 (0.55)
$CC_{1/2}$	99.9 (78.9)	99.9 (41.6)	99.8 (81.9)
I/σ(I)	27.6 (2.8)	18.3 (1.2)	17.4 (3.6)
Wilson B-factor ($Å^2$)	334	502	247
Refinement			
Reflections used all (free)		13211 (688)	
R-work		0.258 (0.332)	
R-free		0.2988 (0.347)	
Ligand atoms		18	
Protein residues		1173	
RMS (bonds)		0.004	
RMS (angles)		0.838	
Ramachandran favored (%)		96.9	
Ramachandran allowed (%)		2.9	
Ramachandran outliers (%)		0.2	
Clashscore		12.58	
Overall score		1.92	
Average B-factor ($Å^2$)		315.5	

Values in parentheses refer to the indicated resolution shell.

*Hp*DnaG^{HBD}. ATP hydrolysis was measured using the previously described spectrophotometric method (37) based on the coupling of ATP hydrolysis to the oxidation of NADH with pyruvate kinase and lactate dehydrogenase. The hydrolysis rates presented correspond to the mean of three independent experiments performed with each sample.

DNA binding

Equilibrium DNA binding assays were performed on a Clariostar (BMG Labtech) microplate reader, fitted with polarization filters to measure fluorescence anisotropy. The binding assays were conducted in 384-well plates at room temperature in 40 μl reaction volumes in 20 mM Hepes pH 7.5, 5 mM $MgCl_2$, 50 mM potassium acetate and 5% (v/v) glycerol supplemented with 0.2 $mg.ml^{-1}$ BSA and 0.5 mM AMPPNP or ATP. 0 to 100 nM *Hp*DnaB, *Hp*DnaB•*Hp*DnaG^{HBD} complex, or 0 to 15 μM *Hp*DnaG^{HBD} were titrated into 1 nM 5′-FAM-labeled 20mer dsDNA composed of oligonucleotides 5′- GACTACGTACTGTTACGTCT-3′ and 5′-AGACGTAACAGTACGTAGTC-3′ or 1 nM 5′-FAM-labeled 20mer polydT ssDNA oligonucleotide. After subtracting the polarization values obtained for DNA alone, the mean data from three independent experiments were fitted to a standard binding equation ($y = Bmax*x^h/(Kd^h+x^h)$) assuming a single binding site with Hill slope (h) using GraphPad Prism6. The fits were very good, with R^2 values all above 0.98 (Supplementary Table S1).

DNA unwinding assay

Unwinding of forked DNA was carried out by first annealing a 5′-FAM-labeled oligonucleotide (5′-FAM-TACGTAACGAGCCTGC$(dT)_{25}$–3′) to a 1.1 molar excess of a 3′ dabcyl quencher-labeled strand (5′-$(dT)_{25}$-GCAGGCTCGTTACGTA-Dabcyl-3′). A capture oligo (5′-GCAGGCTCGTTACGTA-3′) complementary to the base-paired region of the FAM-labeled strand was added to all reactions to prevent reannealing of the unwound substrate. 80 μl reactions containing 50 nM *Hp*DnaB dodecamer (with or without 7.3 μM *Hp*DnaG^{HBD}) and 100 nM fork substrate in helicase buffer (10 mM Tris pH 8.0, 50 mM NaCl, 1% glycerol and 5 mM $MgCl_2$) were started by addition of 100 nM capture DNA and 2 mM ATP and were monitored at 37°C for 3 h using a Clarisotar (BMG Labtech) fluorescence plate reader. Reactions were performed in triplicate and presented data correspond to the average of at least three independent measurements.

RESULTS

Crystal structure of *Hp*DnaB

Crystals of N-terminally 6-histidine-tagged *Hp*DnaB (His-*Hp*DnaB) diffracted to 6.7 Å resolution and belonged to

the high symmetry space group $I2_13$. The structure was solved by the single anomalous dispersion method and the final model was refined to an R_{factor}/R_{free} of 0.25/0.29 with very good geometry (Supplementary Figure S3A, B and Table 1). Given the low resolution, SeMet-substituted protein crystals were grown and used to collect a single wavelength data set at the Se edge to ascertain the position of the methionines in the structure. An anomalous difference Fourier map confirmed the correct location of modeled methionines leaving no ambiguity regarding the position of the subdomains of His-*Hp*DnaB (Supplementary Table S2 and Figure S3C).

The crystal structure consists of two His-*Hp*DnaB homodimers (chains AB and CD) per asymmetric unit. While chains A and B comprise both the NTD and CTD, chains C and D display only the NTD. Two hexamers, each of which is composed of three homodimers, are generated with the operation of a crystallographic three-fold symmetry (Supplementary Figure S3A). As a result, hexamer 1 consisting of three copies of chains AB is complete with both NTD- and CTD-rings, while hexamer 2 consisting of three copies of chains CD has only the NTD-ring. The absence of the CTD-ring in hexamer 2 cannot be accounted for by protein degradation, since *Hp*DnaB was intact in the crystals (Supplementary Figure S3D). Instead, analysis of the crystal packing indicates that the entire CTD-ring 2 is in a large solvent channel. A model of the complete dodecamer was generated by superimposing a copy of hexamer 1 onto the NTD-ring 2 (Figure 1B). The complete dodecamer measures 190 Å in length and 120 Å in diameter (Figure 1B). When this model is used to generate the crystal lattice, no clashes were observed between symmetry-related molecules and the subunits closest to the CTD-ring 2 are at 25 Å (Sup. Movie M1). This demonstrates that the solvent channel is sufficiently large to accommodate the CTD-ring 2. Given that no particular flexibility of the CTD was detected in EM studies (17), we concluded that the absence of density for the CTD-ring 2 is due to rigid-body movements of individual CTDs permitted by the high crystal solvent content (70%) and the lack of crystal contact in this area.

*Hp*DnaB forms a stack-twisted double hexamer

The structure of His-*Hp*DnaB reveals that the last two helices of the NTD fold into a helical hairpin that mediates NTD dimer formation (Figure 1C and Supplementary Figure S3B) as in all DnaB structures (3,4,38). The two NTD-rings of His-*Hp*DnaB are identical and composed of a planar trimer of dimers delimiting a 50 Å wide channel, a state recently described as 'dilated', found in apo DnaBs (3,4,38,39) (Figure 1C). The NTD-rings stack on each other, and if the two hexamers are projected onto the same plane, the vectors through the center-of-mass are offset by 60 degrees (Figure 1C). These two hexamers can be described as a 'stack-twisted' assembly. Strikingly, the arrangement adopts an apparent six-fold symmetry when observed from the top thus explaining the six-fold symmetry detected in our previous negative staining electron microscopy (nsEM) reconstruction (17). The interactions of the NTD-rings are mediated by head domains associations, burying a total surface of ∼1400 Å^2. Helices α1 and α5 of chain A engage α1 of chain D and α5 of chain C (NTD-ring 2), respectively, and chain B (NTD-ring 1) interacts with chain C via α1–α1 interactions (Figure 2A). Although the low resolution of the structure does not allow for a precise description of the dodecamer interface, α1–α1 interactions seem predominantly hydrophobic, involving the first residues of the helix.

The structural basis for the connection between the CTD subunits is the same as in other DnaB structures, with each linker helix inserted in the hexamerisation pocket of the adjacent ATPase domain (Figure 1B,C) (3–5). The CTD-ring adopts a pseudo six-fold symmetry with a closed-ring similar to GP40 (Figure 1C) (3,4). One feature that we identified previously in the structure of the isolated *Hp*DnaB^{CTD} is a large insertion (named HPI for *Helicobacter pylori* insertion) within the ATPase domain forming a helix-turn-helix composed of α15 and α16 (Figure 1B,C). In the dodecameric crystal structure, the HPI helices from chain A and chain B undergo important conformational changes resulting in different structures compared to the HPI of the *Hp*DnaB^{CTD} structure (17). In chain A, α16 and the N-terminal portion of α15 are ordered while the situation is inverted in chain B with α15 and the C-terminal part of α16 ordered (Figure 1C and Supplementary Figure S4). As anticipated from the nsEM structure, the HPIs form a collar extending the CTD-ring (Figure 1B,C). Interestingly, α15 of chain A (but not of chain B) interacts with the adjacent ATPase domain. This feature suggests a structural explanation for some of the unusual properties of *Hp*DnaB. In contrast with other DnaBs, *Hp*DnaB maintains both ATPase and helicase activities in the absence of the NTD head domain (40). The structure of the His-*Hp*DnaB dodecamer suggests that interaction of the HPI collar with the ATPase domain could stabilize the CTD-ring in the absence of NTD during DNA unwinding and/or translocation experiments. This is also supported by the fact that a HPI-deleted *Hp*DnaB mutant protein does not form hexamers and is inactive for ATP hydrolysis and DNA unwinding (40).

Dynamics of *Hp*DnaB in solution

We observed that in the crystal structure, some residues of the N-terminal His-tag are located at the NTD–NTD interface (Figure 2A). Concerned by the fact that the His-tag might influence the oligomeric state of *Hp*DnaB as seen in other hexameric AAA+ ATPases (41), we purified the protein without the His-tag (named *Hp*DnaB hereafter). Size-Exclusion Chromatography coupled with Multi-Angle Static Light Scattering (SEC-MALS) experiments showed that *Hp*DnaB elutes as a single peak and has a mass of around 585 kDa. This molecular mass is lower than the expected *Hp*DnaB dodecamer (669 kDa) suggesting that the protein assembly might be in equilibrium between hexamer and dodecamer. Online size exclusion chromatography coupled to small angle X-ray scattering (SAXS) was used to determine the radius of gyration (Rg) of the proteins. Rgs obtained for His-*Hp*DnaB and *Hp*DnaB are comparable (67.4 Å and 66.7 Å, respectively; Supplementary Table S3). Rgs calculated from the model of the *Hp*DnaB hexamer or dodecamer based on our crystal structure are 46.8 Å and 65.5 Å, respectively (Table 2, see also Figures S1 and S2). Thus,

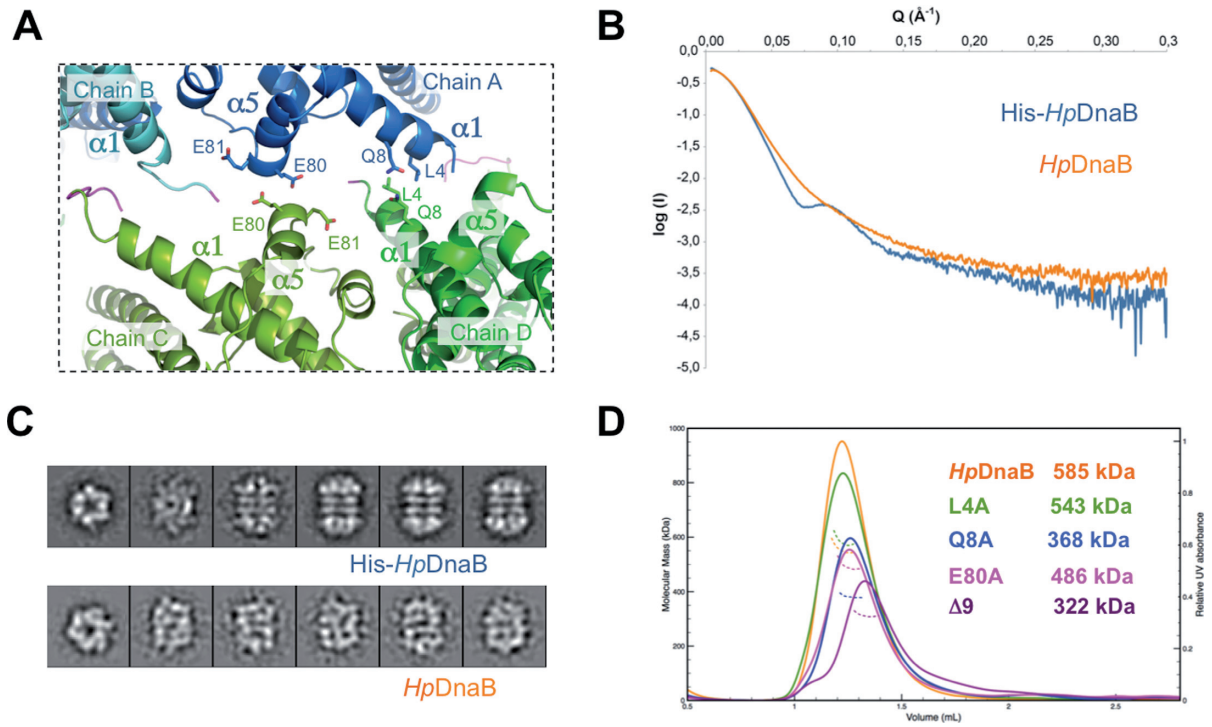

Figure 2. Conformation of the dodecamer and site-directed mutagenesis study of the hexamer–hexamer interface. (**A**) Close-up view of the hexamer–hexamer interface with side chains of participating residues shown as sticks. Helices are labeled and the histidine-tag is colored in magenta. (**B**) Experimental SAXS curves of His-*Hp*DnaB (blue) and *Hp*DnaB (orange). (**C**) Representative reference-free 2D class averages of His-*Hp*DnaB and *Hp*DnaB. (**D**) Size exclusion chromatograms (280 nm) of *Hp*DnaB and mutants L4A, Q8A, E80A, and Δ9 performed on a Superdex 200 increase (GE, 0.45 ml.min^{-1}). MALS weight-averaged molar masses are indicated as dotted lines.

our SAXS data clearly demonstrate that His-*Hp*DnaB and *Hp*DnaB are both predominantly dodecameric in solution.

We noticed that the scattering curves of the two proteins were nonetheless different, with the His-*Hp*DnaB curve exhibiting a dip and hump between Q values of 0.07 to 0.09 (Figure 2B). This feature has previously been found in ring shape helicases in solution, including *Ec*DnaB (5,42). This feature is absent in the *Hp*DnaB SAXS curve, suggesting that *Hp*DnaB is more dynamic and that the shapes of the two dodecameric particles are different. By comparing the SAXS profiles with a theoretical SAXS curve of the dodecamer model, we observed that the stack-twisted dodecamer fits better the His-*Hp*DnaB SAXS curve ($\chi^2 = 11.8$) than the *Hp*DnaB curve ($\chi^2 = 23.6$). Both fits were improved by using multi-ensemble searches (MES, i.e. a combination of different structures (36)). A better fit was obtained for His-*Hp*DnaB data ($\chi^2 = 8.8$) using a combination of 91% of dodecamer and 9% of hexamer (Supplementary Figure S5A) and for *Hp*DnaB data ($\chi^2 = 14.1$) using a combination of 75% of dodecamer and 25% of hexamer (Supplementary Figure S5B).

To gain further insights into the organization of *Hp*DnaB dodecamers, nsEM images of a *Hp*DnaB sample were compared with the previously obtained His-*Hp*DnaB images (17). As in the case of His-*Hp*DnaB, class averages of *Hp*DnaB confirm the presence of four-layered particles, but the symmetry is less obvious than for His-*Hp*DnaB (Figure 2C). No 3D reconstruction was attempted at this stage because, in contrast to His-*Hp*DnaB, multivariate statistical analysis did not reveal any clear cyclic or dihedral symmetry. Nevertheless, the obtained classes suggest that the *Hp*DnaB dodecamer also relies on NTD–NTD interactions.

To determine if the interface between the NTD-rings seen in the crystal structure of His-*Hp*DnaB is also relevant in *Hp*DnaB, we generated a series of structure-guided mutants. An N-terminal deletion mutant starting at residue 10 (*Hp*DnaB$^{\Delta 9}$) and two point mutants L4A (*Hp*DnaB^{L4A}) and Q8A (*Hp*DnaB^{Q8A}) were constructed to disrupt the contacts between α1 helices. Another mutant, E80A (*Hp*DnaB^{E80A}) was designed to target the α5–α5 interaction. SEC-MALS experiments performed on the purified *Hp*DnaB mutants showed that the mass of the *Hp*DnaB$^{\Delta 9}$ was 322 kDa, so closer to that of a hexamer (334 kDa) (Figure 2D). In comparison, single mutants *Hp*DnaB^{L4A}, *Hp*DnaB^{E80A} and *Hp*DnaB^{Q8A} had a mass of 543, 486 and 368 kDa, respectively. So, the dodecamer–hexamer equilibrium previously observed in *Hp*DnaB MALS measurement was clearly affected in mutants *Hp*DnaB$^{\Delta 9}$, *Hp*DnaB^{Q8A}, *Hp*DnaB^{E80A} but not in *Hp*DnaB^{L4A}. The oligomeric states of wild-type and mutants *Hp*DnaBs were then compared using chemical cross-linking (Supplementary Figure S6). *Hp*DnaB in complex with AMPPNP and ssDNA, which forms hexamers (see after), was used as a control. In the presence of cross-linking agent, *Hp*DnaB and *Hp*DnaB^{L4A} formed assemblies of the same size and larger than a hexamer, while the mutants *Hp*DnaB$^{\Delta 9}$, *Hp*DnaB^{Q8A} and to a less extent *Hp*DnaB^{E80A}

Table 2. Summary of the oligomeric states of *Hp*DnaB and associated complexes studied

	MALS		SAXS		
	MW (kDa)	*Hp*DnaB *oligomer*	Rg (Å)	Dmax (Å)	*Hp*DnaB *oligomer*
His-*Hp*DnaB	687	***12***	67.4	234	***12***
*Hp*DnaB	585	***6–12***	66.7	228	***12***
*Hp*DnaB + ATP	546	***6–12***	67.9	234	***12***
*Hp*DnaB + ATP + ssDNA	553	***6–12***	68.0	235	***12***
*Hp*DnaB + AMPPNP	500	***6–12***	67.6	234	***12***
*Hp*DnaB + AMPPNP + ssDNA	310	***6***	47.0	146	***6***
*Hp*DnaB + *Hp*DnaG^{HBD}	345	***6*** (+ x *Hp*DnaG^{HBD})	55.0	193	***6*** (+ *3* *Hp*DnaG^{HBD})
Theoretical values[#]	**MW (kDa)**		**Rg (Å)**	**Diameter (Å)**	
*Hp*DnaB hexamer	334	***6***	46.8	147	***6***
*Hp*DnaB dodecamer	669	***12***	65.5	207	***12***
*Hp*DnaB$_6$•*Hp*DnaG$^{HBD}{}_3$[‡]	385		50.7	152	

MW: Molecular weight; x = 1, 2 or 3; [‡] Model obtained using *Bst*DnaB$_6$• *Bst*DnaG$^{HBD}{}_3$ structure (pdb code 2R6A) as template, [#] Theoretical Rg and diameter values were obtained using CRYSOL (49).

formed predominantly hexamers (Supplementary Figure S6). These results are in agreement with MALS measurements. Collectively these experiments demonstrate that mutations targeting the interface seen in the crystal structure affect dodecamer formation of *Hp*DnaB. We concluded that the structure of *Hp*DnaB in solution is similar to the one seen in the crystal structure and that α1 is essential for hexamer–hexamer assembly. However in the absence of the His-tag, *Hp*DnaB probably adopts multiple conformations, some of which might trigger dissociation of the two hexamers. Our data suggest that the N-terminal His-tag reduces the dynamics of the protein, possibly explaining that only the His-tagged protein crystallized. This is also supported by the observation that the values of Rg derived from the SAXS are more stable across the peak of His-*Hp*DnaB than across the peak of *Hp*DnaB (Supplementary Figure S1).

*Hp*DnaB binds ssDNA but not dsDNA

Since DnaBs are loaded onto ssDNA at replication forks and *Hp*DnaB is able to translocate in the 5′ to 3′ direction (40), we investigated the fate of the double ring on DNA. Using fluorescence anisotropy, we found that *Hp*DnaB interacts with a 20mer polydT (20dT) ssDNA oligonucleotide in the presence of ATP or the non-hydrolysable ATP analogue, AMPPNP, with dissociation constants (K_D) of 15 ± 1 nM and 3.1 ± 0.1 nM, respectively, but not in the absence of nucleotide (Figure 3A). In contrast, no or very weak binding was observed with dsDNA even in the presence of nucleotides (Figure 3A). Increasing the length of the ssDNA oligonucleotide (Figure 3B) barely increased the binding affinity in the presence of AMPPNP (K_D = 1.8 ± 0.2 nM) and instead reduced the binding affinity of *Hp*DnaB in the presence of ATP (K_D = 70 ± 6 nM). The binding of *Hp*DnaB to ssDNA was found to be cooperative in the presence of AMPPNP, but not in the presence of ATP (Supplementary Table S1), indicating that the DNA binding mode may be affected by the nucleotide-bound state of *Hp*DnaB.

Next, the complexes formed by *Hp*DnaB and ssDNA were analyzed by SEC-MALS in the presence of either ATP or AMPPNP. The elution profile and the estimated molecular weight of *Hp*DnaB in the presence and absence of 75 μM ssDNA were very similar when 0.5 mM ATP was added to the buffer (Figure 3C). In both cases, the mass of *Hp*DnaB derived from the MALS was around 550 kDa thus corresponding to the mostly dodecameric *Hp*DnaB (Figure 3B). When SAXS data were collected on the same sample and in the same size exclusion chromatography conditions, the Rgs of *Hp*DnaB•ATP and *Hp*DnaB•ATP•20dT samples were 67.9 Å and 68.0 Å, respectively (Supplementary Table S2). Together these data suggest that the complex *Hp*DnaB•ATP•20dT is a dodecamer. In contrast, in the presence of AMPPNP, the addition of 45 μM of 20dT to the sample resulted in the reduction of the peak corresponding to the *Hp*DnaB dodecamer and the appearance of second and third peaks at later elution volumes. The second peak contained *Hp*DnaB and had a molecular weight of 310 kDa (Figure 3D). The addition of 75 μM of 20dT to the *Hp*DnaB•AMPPNP sample resulted in the complete disappearance of the dodecamer peak. Interestingly, the Rg derived from the SAXS analysis of the sample corresponding to the second peak containing the *Hp*DnaB•AMPPNP•20dT was 47.0 Å, corresponding to a hexamer while in the presence of AMPPNP alone, the Rg of *Hp*DnaB was 67.6 Å and corresponds to a dodecamer (Table 2).

Altogether, our results show that *Hp*DnaB binds ssDNA with high affinity in the presence of nucleotides both as a hexamer and a dodecamer. *Hp*DnaB in its ATP-bound state remains a dodecamer when binding to ssDNA, while when ATP hydrolysis is prevented by incubating the complex with AMPPNP, *Hp*DnaB binds ssDNA cooperatively as a hexamer (Table 2 and Supplementary Table S1) (5,12).

*Hp*DnaB interaction with *Hp*DnaG^{HBD} dissociates double rings into hexamers

We investigated the oligomeric state of *Hp*DnaB during formation of the *Hp*DnaB•*Hp*DnaG complex. The crystal structure of the *Bst*DnaB•*Bst*DnaG^{HBD} revealed that each of the three DnaG^{HBD} engages the NTD dimer via interactions with the head domains of *Bst*DnaB (4). To gain insight into the assembly of the primosome of *H. pylori* we analyzed the *Hp*DnaB•*Hp*DnaG^{HBD} complex obtained by mixing the two proteins together using SEC-MALS and

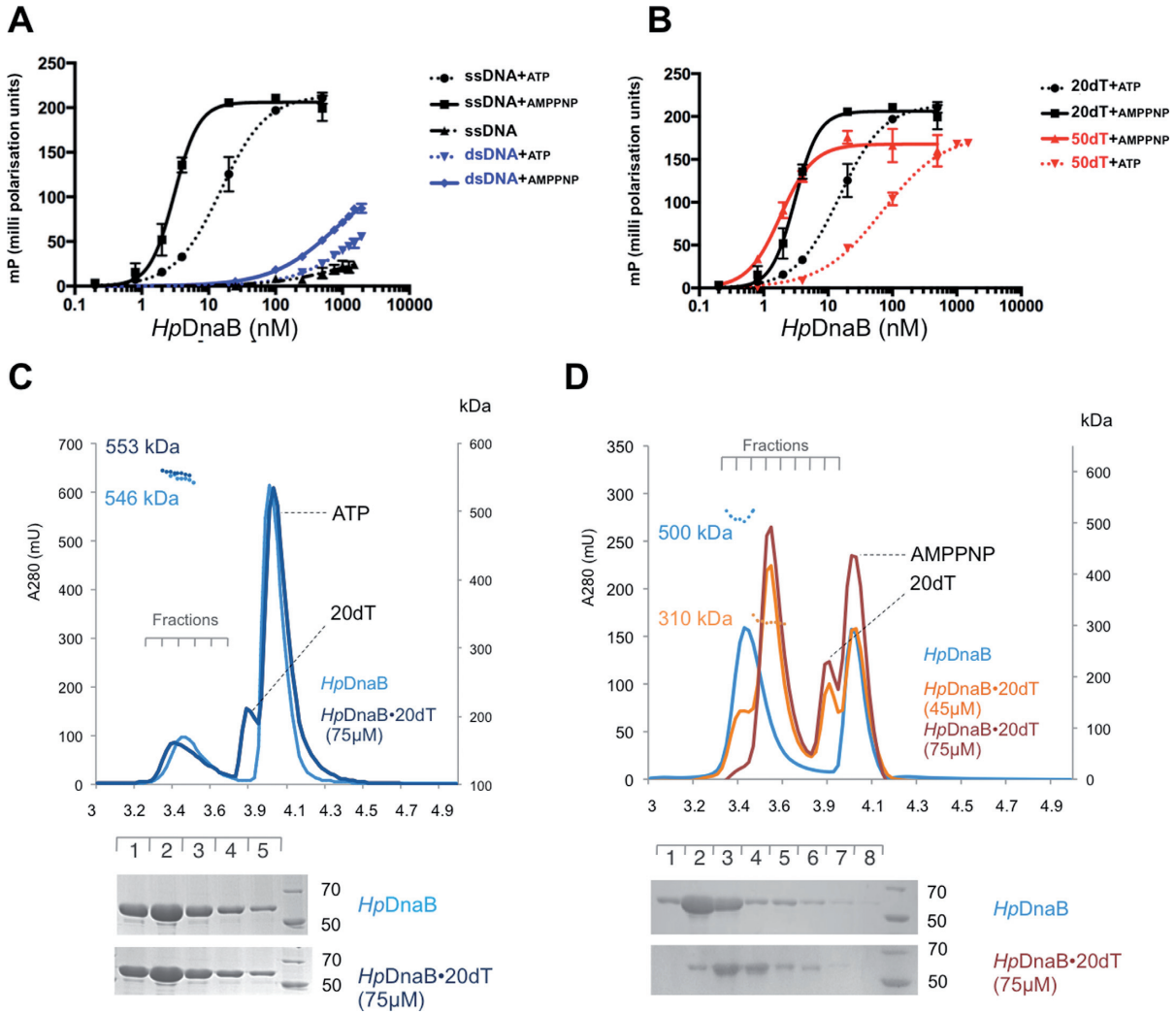

Figure 3. Effects of ATP and AMPPNP on the *Hp*DnaB interaction with DNA. (**A**) Fluorescence anisotropy measurements of *Hp*DnaB binding to either 5′- FAM labeled 20mer ssDNA (20dT) or dsDNA in the presence and absence of nucleotide (ATP and AMPPNP). The curves represent the mean of three independent experiments. (**B**) Similar experiments performed with 5′- FAM labeled 50mer ssDNA (50dT). (**C**) Size exclusion chromatograms (280 nm) of *Hp*DnaB alone (light blue) or mixed with a 20dT oligonucleotide (75 μM) and 5 mM ATP (dark blue). MALS weight-averaged molar masses are indicated as dotted lines. The SDS-PAGE analysis shows the *Hp*DnaB protein elution fractions. (**D**) SEC-MALS experiment performed as in C) except that *Hp*DnaB was incubated with 5 mM AMPPNP and the running buffer contained 0.5 mM AMPPNP. Three samples were analyzed: *Hp*DnaB (blue) and *Hp*DnaB with 45 μM (orange) or 75 μM (red) 20dT. The SDS-PAGE analysis shows that *Hp*DnaB elutes slightly later in the presence of ssDNA and AMPPNP.

SAXS. SEC experiments showed that this complex eluted as two peaks and SDS-PAGE showed that the first peak contained both *Hp*DnaB and *Hp*DnaG^{HBD}, while the second contained exclusively *Hp*DnaG^{HBD} (Figure 4A). Measurements of the molecular weight by MALS indicated that the peak corresponding to the *Hp*DnaB•*Hp*DnaG^{HBD} complex had a molecular mass of approximately 345 kDa, suggesting that this peak corresponds to hexameric rather than dodecameric *Hp*DnaB (the theoretical mass of the hexamer is 334 kDa) with one or perhaps more *Hp*DnaG^{HBD} (17 kDa) molecules bound. *Hp*DnaG^{HBD} alone had a mass of around 35 kDa corresponding to a dimer as previously observed (43).

SAXS data corroborated these observations with the complex *Hp*DnaB•*Hp*DnaG^{HBD} having an Rg of 55.0 Å, much lower than a dodecamer (66.7 Å) but greater than a theoretical *Hp*DnaB hexamer (46.8 Å) (Supplementary Table S3). We then modeled the *Hp*DnaB$_6$•*Hp*DnaG$^{HBD}{}_3$ complex using the crystal structures of His-*Hp*DnaB and *Hp*DnaG^{HBD} and the *Bst*DnaB$_6$•*Bst*DnaG$^{HBD}{}_3$ crystal structure as a template (43). A very good fit of the experimental SAXS profile was obtained with the theoretical curve derived from the *Hp*DnaB$_6$•*Hp*DnaG$^{HBD}{}_3$ model (χ^2 = 5.8) compared with the curve derived from the *Hp*DnaB dodecamer (χ^2 = 36.8) (Figure 4B). When using MES, the fit was significantly improved with a mixture of 89% of the *Hp*DnaB$_6$•*Hp*DnaG$^{HBD}{}_3$ complex and of 11% of *Hp*DnaB dodecamer (χ^2 = 3.5; Figure 4B), suggesting that the peak observed in SEC-MALS contains both uncomplexed dodecameric *Hp*DnaB and hexameric *Hp*DnaG^{HBD}-bound *Hp*DnaB. Together, these data reveal that formation of the *H. pylori* primosome results in the dissociation of the helicase dodecamer into hexamers that can interact with up

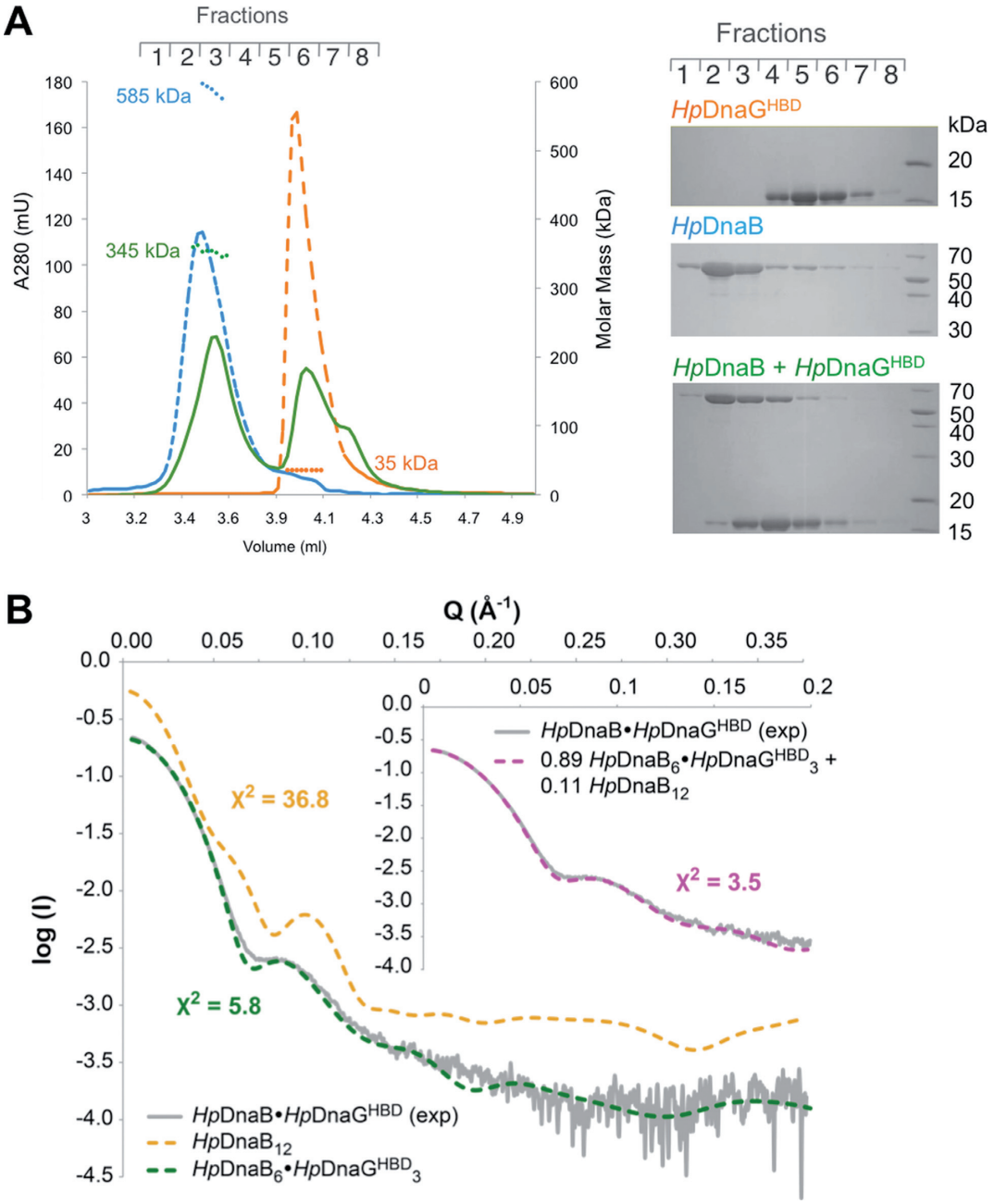

Figure 4. Interaction of *Hp*DnaG^{HBD} dissociates *Hp*DnaB dodecamer. (**A**) Size-exclusion chromatograms (280 nm) of *Hp*DnaB (light blue), *Hp*DnaG^{HBD} (orange) or the reconstituted primosome *Hp*DnaB + *Hp*DnaG^{HBD} (green). MALS weight-averaged molar masses measurements are indicated as dotted lines. The SDS-PAGE analysis shows the proteins contained in the elution fractions. (**B**) Experimental scattering curve of the *Hp*DnaB•*Hp*DnaG^{HBD} peak (grey) compared to theoretical curves of *Hp*DnaB dodecamer (orange), and model of the *Hp*DnaB$_6$•*Hp*DnaG$^{HBD}{}_3$ (green). The inset shows the improved fit obtained from a MES containing a mixture of *Hp*DnaB$_6$•*Hp*DnaG$^{HBD}{}_3$ and *Hp*DnaB dodecamer models.

to three *Hp*DnaG^{HBD} in a conformation similar to the crystal structure of *Bst*DnaB$_6$• *Bst*DnaG$^{HBD}{}_3$ (Table 2).

*Hp*DnaG^{HBD} interacts with *Hp*DnaB and ssDNA to prime helicase and ATPase activities

A major role of primosome formation is the modulation of primase and helicase activities (14,44–46). As for other DnaBs, the ATPase activity of *Hp*DnaB has previously been shown to be stimulated by *Hp*DnaG^{HBD} or by ssDNA (17,40). We have thus investigated the effect of *Hp*DnaG^{HBD} on the ability of *Hp*DnaB to hydrolyse ATP, bind DNA and unwind forked DNA duplexes. *Hp*DnaB had an ATPase activity of 0.04 ± 0.03 μM ATP.s^{-1} at a concentration of 500 nM (Supplementary Table S4). As expected, addition of *Hp*DnaG^{HBD} or ssDNA increased the ATPase activity of *Hp*DnaB approximately three-fold (Supplementary Table S4). The activity was increased almost eight-fold by adding both ssDNA and *Hp*DnaG^{HBD}, suggesting that the

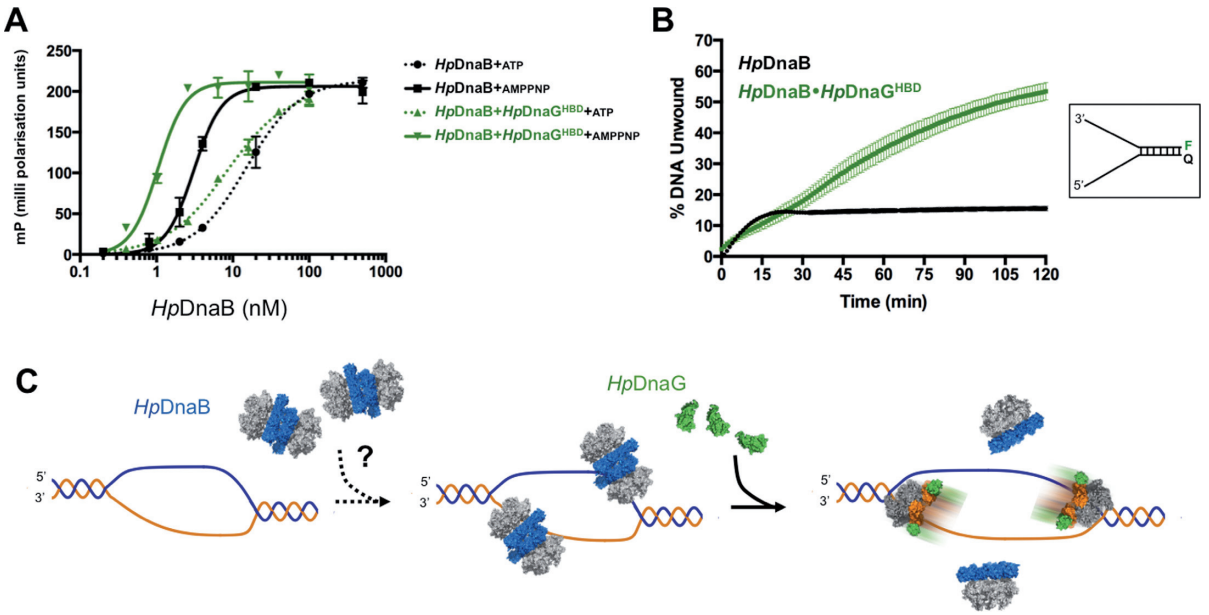

Figure 5. *Hp*DnaG^{HBD} primes *Hp*DnaB activities. (**A**) Single-stranded DNA binding activity of *Hp*DnaB and *Hp*DnaB•*Hp*DnaG^{HBD} complex in the presence of ATP (0.5 mM) or AMPPNP (0.5 mM) as measured by fluorescence anisotropy. (**B**) Unwinding of a fluorophore (F)/quencher (Q)-labeled forked DNA substrate (shown schematically in inset) by *Hp*DnaB (black) or *Hp*DnaB•*Hp*DnaG^{HBD} (green). The curve represents the mean of three independent experiments and the standard deviations are indicated for each measurement as error bars. (**C**) Schematic illustration of the proposed model of *Hp*DnaG^{HBD} activation of the double hexamer on ssDNA during replication initiation in *Helicobacter pylori*.

ternary complex is the most active for ATP hydrolysis with a hydrolysis rate of 0.35 ± 0.08 μM ATP.s^{-1} (Supplementary Table S4).

The binding affinity of these proteins to ssDNA was then measured by fluorescence anisotropy. The *Hp*DnaB·*Hp*DnaG^{HBD} complex exhibited a higher affinity for ssDNA than *Hp*DnaB alone in the presence of ATP (K_D = 8.3 ± 0.6 nM versus 15 ± 1 nM) or AMPPNP (K_D = 1.0 ± 0.1 versus 3.1 ± 0.1 nM) (Figure 5A). *Hp*DnaG^{HBD} thus increases the affinity of *Hp*DnaB for ssDNA in the presence of nucleotides. Interestingly, *Hp*DnaG^{HBD} alone interacts with ssDNA, but with an affinity in the micromolar range (Supplementary Figure S7). Translocation of the double hexamer on ssDNA poses several mechanistic problems. (i) *Hp*DnaB unwinds dsDNA in the 5′ to 3′ direction, so only one hexamer can be active; (ii) the second (inactive) hexamer would considerably hinder the first one's activity by binding non-specifically to ssDNA via its DNA binding loops; (iii) an inactive hexamer would represent a significant inert mass to be translocated by the active one. This suggests that for efficient helicase activity, a double hexamer would have to be separated to release the correctly positioned *Hp*DnaB hexamer. To test this hypothesis we analyzed the helicase activity of *Hp*DnaB in the presence and absence of *Hp*DnaG^{HBD}. We used a fluorescence-based assay similar to the one used previously to measure *Ec*DnaB·*Ec*DnaC helicase activity (10). A forked DNA substrate was formed by annealing an oligonucleotide bearing a 3′ ssDNA tail and a fluorescein label at its 5′ end with a complementary oligonucleotide bearing a 5′ ssDNA tail and a quenching dye (Dabcyl) at its 3′ end. As seen in Figure 5B, double hexameric *Hp*DnaB displayed weak DNA unwinding activity, rapidly reaching a maximum of only 10% DNA unwound. In contrast, in complex with *Hp*DnaG^{HBD}, *Hp*DnaB was able to unwind dsDNA, reaching 60% DNA unwound. The initial rates of DNA unwinding were very similar in both cases, confirming that *Hp*DnaB is indeed an active DNA helicase, but the activity of the enzyme was drastically affected by the presence of the primase *Hp*DnaG^{HBD}. No more activity was detected for *Hp*DnaB alone after approximately 20 min, whereas in the presence of *Hp*DnaG^{HBD}, helicase activity could still be detected 2 h after the start of the reaction.

DISCUSSION

DNA replication relies on replicative helicases to initiate progression of replication forks and to anchor the primase. While most DnaBs characterized to date have been reported to be hexameric, we previously found that *Hp*DnaB from *H. pylori* was able to form double hexamers, thus questioning how this structure would assemble and function on replication forks. In this study, we have addressed the structural mechanisms of *Hp*DnaB activation during primosome formation on ssDNA.

The crystal structure of the *Hp*DnaB dodecamer solved here provides significant information on *Hp*DnaB dodecamer compared to our previous nsEM reconstruction (17). It reveals that the NTDs of the helicase are arranged in dilated collars that self-interact in a stack-twisted mode to generate a head-to-head double hexamer. The dodecamer assembly stabilizes the NTD-ring conformation but allows for the CTD-ring to remain sufficiently dynamic to accept structural changes associated with ATP hydrolysis or ssDNA binding. Our work establishes that if the topology of this bacterial dodecameric helicase (i.e. NTD–NTD in-

teractions) is reminiscent of Mcm2–7 and some MCMs, the structural and molecular determinants of the hexamers association are different. In *Methanobacterium thermoautotrophicum* MCM (*Mt*MCM) (47), dodecamerization relies on interactions between loops that coordinate Zn atoms in the *Mt*MCM B domain (Supplementary Figure S8). The structural basis for dodecamer formation is completely different in *Hp*DnaB (Figure 2) and thus rules out a common evolutionary structural motif. Nevertheless, it is interesting to note that, despite diverse evolutionary routes, dodecameric replicative helicases might exist in all kingdoms of life, suggesting that some selective advantages might be associated with this organization (48).

It is as yet unclear how *Hp*DnaB is loaded onto the replication forks and if an additional factor is required for this process (Figure 5C). In this regard, we found that the double hexameric *Hp*DnaB does not interact efficiently with dsDNA contrary to ssDNA, suggesting that unwound origins of replication might be better substrates (Figure 3A). The *Hp*DnaB dodecamer positions two hexamers in opposite directions but the two rings cannot unwind dsDNA simultaneously in the 5′ to 3′ direction if a single strand passes through the double ring. Accordingly, the use of a longer ssDNA oligonucleotide did not increase the affinity of the *Hp*DnaB for DNA, suggesting that only one of the two rings of the dodecamer is efficiently bound to ssDNA (Figure 3B).

We found that the *Hp*DnaB dodecamer is indeed poorly active for DNA unwinding and that the protein unwinds dsDNA as a hexamer, similar to other DnaBs (12). ATP hydrolysis and ssDNA binding are not sufficient to separate the two rings (Figure 3C and Table 2), suggesting that an additional factor is required to initiate DNA unwinding at the replication fork. Our study suggests that the primase might be such a factor since the interaction with *Hp*DnaG^{HBD} separates the *Hp*DnaB double hexamer (Figures 3D, 5C and Table 2). This can be explained by the crystal structure of His-*Hp*DnaB in which the dodecamer interface mediated by NTD collars overlaps the primase interaction site described in *Bst*DnaB (4) and conserved in *Hp*DnaB (43). *Hp*DnaG association with *Hp*DnaB not only separates the dodecamer, but also increases its ATPase activity, its affinity for ssDNA and its DNA unwinding capacity. These findings suggest that the separation of the dodecamer by *Hp*DnaG drives DNA unwinding by one hexamer in the 5′ to 3′ direction allowing replication to initiate (Figure 5C). Mechanistically, the separation of the two helicase rings by interaction with the primase might also be relevant to other systems such as archaeal or eukaryotic systems, which also exploit double ring helicases during replication initiation.

SUPPLEMENTARY DATA

Supplementary Data are available at NAR Online.

ACKNOWLEDGEMENT

Thanks are due to G. Fox and A. Thompson on beamline PROXIMA2, J. Perez and P. Roblin for help on the SWING beamline from SOLEIL and ESRF staff on beamline ID14EH4. We acknowledge the use of the UMS3444 Protein Science platform, the platforms of the Grenoble Instruct Center (ISBG : UMS 3518).

FUNDING

This work was supported by the ATIP-Avenir program (L.T. and J.T.) of CNRS and by a fellowship Region Rhône-Alpes from the program CIBLE 2011 (A.B.). The Grenoble Instruct Center is supported by FRISBI (ANR-10-INSB-05-02) and GRAL (ANR-10-LABX-49-01) within the Grenoble PSB. The EM facility is supported by the Rhône-Alpes Region, the Fondation Recherche Medicale (FRM), the fonds FEDER, the Centre National de la Recherche Scientifique (CNRS), the CEA, the University of Grenoble, EMBL, and the GIS-Infrastrutures en Biologie Sante et Agronomie (IBISA). Funding for open access charge: CNRS.
Conflict of interest statement. None declared.

REFERENCES

1. Costa,A., Hood,I.V. and Berger,J.M. (2013) Mechanisms for initiating cellular DNA replication. *Annu. Rev. Biochem.*, **82**, 25–54.
2. Bailey,S., Eliason,W.K. and Steitz,T.A. (2007) The crystal structure of the Thermus aquaticus DnaB helicase monomer. *Nucleic Acids Res.*, **35**, 4728–4736.
3. Wang,G., Klein,M.G., Tokonzaba,E., Zhang,Y., Holden,L.G. and Chen,X.S. (2008) The structure of a DnaB-family replicative helicase and its interactions with primase. *Nat. Struct. Mol. Biol.*, **15**, 94–100.
4. Bailey,S., Eliason,W.K. and Steitz,T.A. (2007) Structure of hexameric DnaB helicase and its complex with a domain of DnaG primase. *Science*, **318**, 459–463.
5. Strycharska,M.S., Arias-Palomo,E., Lyubimov,A.Y., Erzberger,J.P., O'Shea,V.L., Bustamante,C.J. and Berger,J.M. (2013) Nucleotide and partner-protein control of bacterial replicative helicase structure and function. *Mol. Cell*, **52**, 844–854.
6. Davey,M.J. and O'Donnell,M. (2003) Replicative helicase loaders: ring breakers and ring makers. *Curr. Biol.*, **13**, R594–R596.
7. Soultanas,P. (2012) Loading mechanisms of ring helicases at replication origins. *Mol. Microbiol.*, **84**, 6–16.
8. Kobori,J.A. and Kornberg,A. (1982) The Escherichia coli dnaC gene product. III. Properties of the dnaB-dnaC protein complex. *J. Biol. Chem.*, **257**, 13770–13775.
9. Karplus,P.A. and Diederichs,K. (2012) Linking crystallographic model and data quality. *Science*, **336**, 1030–1033.
10. Arias-Palomo,E., O'Shea,V.L., Hood,I.V. and Berger,J.M. (2013) The bacterial DnaC helicase loader is a DnaB ring breaker. *Cell*, **153**, 438–448.
11. Liu,B., Eliason,W.K. and Steitz,T.A. (2013) Structure of a helicase-helicase loader complex reveals insights into the mechanism of bacterial primosome assembly. *Nat. Commun.*, **4**, 2495.
12. Itsathitphaisarn,O., Wing,R.A., Eliason,W.K., Wang,J. and Steitz,T.A. (2012) The hexameric helicase DnaB adopts a nonplanar conformation during translocation. *Cell*, **151**, 267–277.
13. Makowska-Grzyska,M. and Kaguni,J.M. (2010) Primase directs the release of DnaC from DnaB. *Mol. Cell*, **37**, 90–101.
14. Bird,L.E., Pan,H., Soultanas,P. and Wigley,D.B. (2000) Mapping protein-protein interactions within a stable complex of DNA primase and DnaB helicase from Bacillus stearothermophilus. *Biochemistry*, **39**, 171–182.
15. Robinson,A., Causer,R.J. and Dixon,N.E. (2012) Architecture and conservation of the bacterial DNA replication machinery, an underexploited drug target. *Curr. Drug Targets*, **13**, 352–372.
16. Soni,R.K., Mehra,P., Mukhopadhyay,G. and Dhar,S.K. (2005) Helicobacter pylori DnaB helicase can bypass Escherichia coli DnaC function in vivo. *Biochem. J.*, **389**, 541–548.
17. Stelter,M., Gutsche,I., Kapp,U., Bazin,A., Bajic,G., Goret,G., Jamin,M., Timmins,J. and Terradot,L. (2012) Architecture of a dodecameric bacterial replicative helicase. *Structure*, **20**, 554–564.

18. Van Duyne,G.D., Standaert,R.F., Karplus,P.A., Schreiber,S.L. and Clardy,J. (1993) Atomic structures of the human immunophilin FKBP-12 complexes with FK506 and rapamycin. *J. Mol. Biol.*, **229**, 105–124.
19. Kabsch,W. (1993) Automatic processing of rotation diffraction data from crystals of initially unknown symmetry and cell constants. *J. Appl. Crystallogr.*, **26**, 795–800.
20. Collaborative Computational Project-4. (1994) The CCP4 suite: Programs for protein crystallography. *Acta Crystallogr.*, **D50**, 760–763.
21. McCoy,A.J., Storoni,L.C. and Read,R.J. (2004) Simple algorithm for a maximum-likelihood SAD function. *Acta Crystallogr. D Biol. Crystallogr.*, **60**, 1220–1228.
22. McCoy,A.J., Grosse-Kunstleve,R.W., Adams,P.D., Winn,M.D., Storoni,L.C. and Read,R.J. (2007) Phaser crystallographic software. *J. Appl. Crystallogr.*, **40**, 658–674.
23. Adams,P.D., Grosse-Kunstleve,R.W., Hung,L.W., Ioerger,T.R., McCoy,A.J., Moriarty,N.W., Read,R.J., Sacchettini,J.C., Sauter,N.K. and Terwilliger,T.C. (2002) PHENIX: building new software for automated crystallographic structure determination. *Acta Crystallogr. D Biol. Crystallogr.*, **58**, 1948–1954.
24. Kashav,T., Nitharwal,R., Abdulrehman,S.A., Gabdoulkhakov,A., Saenger,W., Dhar,S.K. and Gourinath,S. (2009) Three-dimensional structure of N-terminal domain of DnaB helicase and helicase-primase interactions in Helicobacter pylori. *PLoS One*, **4**, e7515.
25. Emsley,P. and Cowtan,K. (2004) Coot: model-building tools for molecular graphics. *Acta Crystallogr. D Biol. Crystallogr.*, **60**, 2126–2132.
26. Cowtan,K. (2010) Recent developments in classical density modification. *Acta Crystallogr. D Biol. Crystallogr.*, **66**, 470–478.
27. Blanc,E., Roversi,P., Vonrhein,C., Flensburg,C., Lea,S.M. and Bricogne,G. (2004) Refinement of severely incomplete structures with maximum likelihood in BUSTER-TNT. *Acta Crystallogr. D Biol. Crystallogr.*, **60**, 2210–2221.
28. Ludtke,S.J., Baldwin,P.R. and Chiu,W. (1999) EMAN: semiautomated software for high-resolution single-particle reconstructions. *J. Struct. Biol.*, **128**, 82–97.
29. Mindell,J.A. and Grigorieff,N. (2003) Accurate determination of local defocus and specimen tilt in electron microscopy. *J. Struct. Biol.*, **142**, 334–347.
30. Heymann,J.B., Cardone,G., Winkler,D.C. and Steven,A.C. (2008) Computational resources for cryo-electron tomography in Bsoft. *J. Struct. Biol.*, **161**, 232–242.
31. Shaikh,T.R., Gao,H., Baxter,W.T., Asturias,F.J., Boisset,N., Leith,A. and Frank,J. (2008) SPIDER image processing for single-particle reconstruction of biological macromolecules from electron micrographs. *Nat. Protoc.*, **3**, 1941–1974.
32. van Heel,M., Harauz,G., Orlova,E.V., Schmidt,R. and Schatz,M. (1996) A new generation of the IMAGIC image processing system. *J. Struct. Biol.*, **116**, 17–24.
33. David,G. and Perez,J. (2009) Combined sampler robot and high-performance liquid chromatography: a fully automated system for biological small-angle X-ray scattering experiments at the Synchrotron SOLEIL SWING beamline. *J. Appl. Crystallogr.*, **42**, 892–900.
34. Konarev,P.V., Volkov,V.V., Sokolova,A.V., Koch,M.H.J. and Svergun,D.I. (2003) PRIMUS: a Windows PC-based system for small-angle scattering data analysis. *J. Appl. Crystallogr.*, **36**, 1277–1282.
35. Schneidman-Duhovny,D., Hammel,M., Tainer,J.A. and Sali,A. (2013) Accurate SAXS profile computation and its assessment by contrast variation experiments. *Biophys. J.*, **105**, 962–974.
36. Pelikan,M., Hura,G.L. and Hammel,M. (2009) Structure and flexibility within proteins as identified through small angle X-ray scattering. *Gen. Physiol. Biophys.*, **28**, 174–189.
37. Panuska,J.R. and Goldthwait,D.A. (1980) A DNA-dependent ATPase from T4-infected Escherichia coli. Purification and properties of a 63,000-dalton enzyme and its conversion to a 22,000-dalton form. *J. Biol. Chem.*, **255**, 5208–5214.
38. Biswas,T. and Tsodikov,O.V. (2008) Hexameric ring structure of the N-terminal domain of Mycobacterium tuberculosis DnaB helicase. *FEBS J.*, **275**, 3064–3071.
39. Lo,Y.H., Tsai,K.L., Sun,Y.J., Chen,W.T., Huang,C.Y. and Hsiao,C.D. (2009) The crystal structure of a replicative hexameric helicase DnaC and its complex with single-stranded DNA. *Nucleic Acids Res.*, **37**, 804–814.
40. Soni,R.K., Mehra,P., Choudhury,N.R., Mukhopadhyay,G. and Dhar,S.K. (2003) Functional characterization of Helicobacter pylori DnaB helicase. *Nucleic Acids Res.*, **31**, 6828–6840.
41. Cheung,K.L., Huen,J., Kakihara,Y., Houry,W.A. and Ortega,J. (2010) Alternative oligomeric states of the yeast Rvb1/Rvb2 complex induced by histidine tags. *J. Mol. Biol.*, **404**, 478–492.
42. Lyubimov,A.Y., Costa,A., Bleichert,F., Botchan,M.R. and Berger,J.M. (2012) ATP-dependent conformational dynamics underlie the functional asymmetry of the replicative helicase from a minimalist eukaryote. *Proc. Natl. Acad. Sci. U.S.A.*, **109**, 11999–12004.
43. Abdul Rehman,S.A., Verma,V., Mazumder,M., Dhar,S.K. and Gourinath,S. (2013) Crystal structure and mode of helicase binding of the C-terminal domain of primase from Helicobacter pylori. *J. Bacteriol.*, **195**, 2826–2838.
44. Johnson,S.K., Bhattacharyya,S. and Griep,M.A. (2000) DnaB helicase stimulates primer synthesis activity on short oligonucleotide templates. *Biochemistry*, **39**, 736–744.
45. Bhattacharyya,S. and Griep,M.A. (2000) DnaB helicase affects the initiation specificity of Escherichia coli primase on single-stranded DNA templates. *Biochemistry*, **39**, 745–752.
46. Wu,C.A., Zechner,E.L. and Marians,K.J. (1992) Coordinated leading- and lagging-strand synthesis at the Escherichia coli DNA replication fork. I. Multiple effectors act to modulate Okazaki fragment size. *J. Biol. Chem.*, **267**, 4030–4044.
47. Fletcher,R.J., Bishop,B.E., Leon,R.P., Sclafani,R.A., Ogata,C.M. and Chen,X.S. (2003) The structure and function of MCM from archaeal M. *Thermoautotrophicum. Nat. Struct. Biol.*, **10**, 160–167.
48. Sclafani,R.A., Fletcher,R.J. and Chen,X.S. (2004) Two heads are better than one: regulation of DNA replication by hexameric helicases. *Genes Dev.*, **18**, 2039–2045.
49. Svergun,D., Barberato,C. and Koch,M.H.J. (1995) CRYSOL - a Program to Evaluate X-ray Solution Scattering of Biological Macromolecules from Atomic Coordinates. *J. Appl. Crystallogr.*, **28**, 768–773.